Supporting Information

Silicon-Hydroborate Composite Electrodes with High Interfacial Stability for NMC811/Silicon Solid-State Batteries

Hugo Braun[1,2], Clea Bürgel[1,3], Edouard Quérel,[1] Arndt Remhof[1,2], Corsin Battaglia[1,3,4]*

[1]Empa, Swiss Federal Laboratories for Materials Science and Technology, 8600 Dübendorf, Switzerland.

[2]Institut für Anorganische und Analytische Chemie, Albert-Ludwigs-Universität Freiburg, 79104 Freiburg, Germany.

[3]Departement of Information Technology and Electrical Engineering, ETH Zurich, 8092 Zurich, Switzerland.

[4]School of Engineering, Institute of Materials, EPFL, 1015 Lausanne, Switzerland.

Corresponding Author

* arndt.remhof@empa.ch

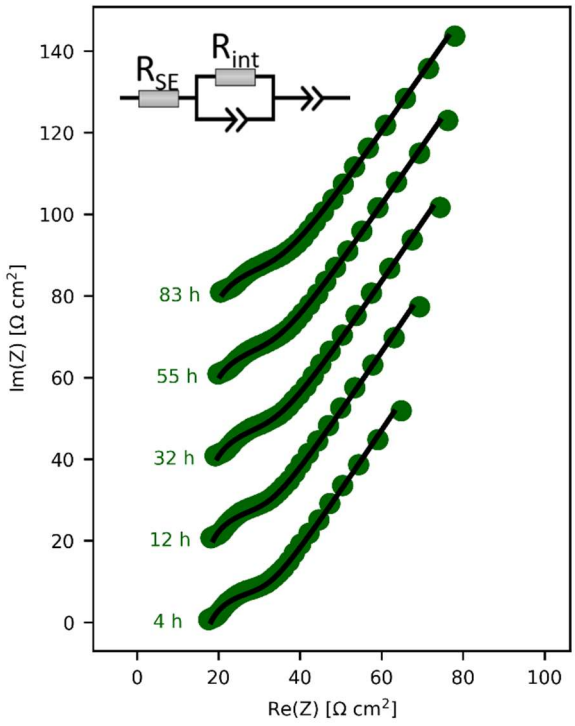

Figure S1. Exemplary impedance spectra of the 3D silicon composite electrode after lithiation to -0.6 V vs In/InLi, i.e. 22 mV vs Li^+/Li, and their fit with the equivalent circuit shown on the top left. Each spectrum is offset on the vertical axis for better readability. The equivalent circuit used for fitting is shown as an insert. The data points used for fitting are shown (from 200 Hz to 5 mHz).

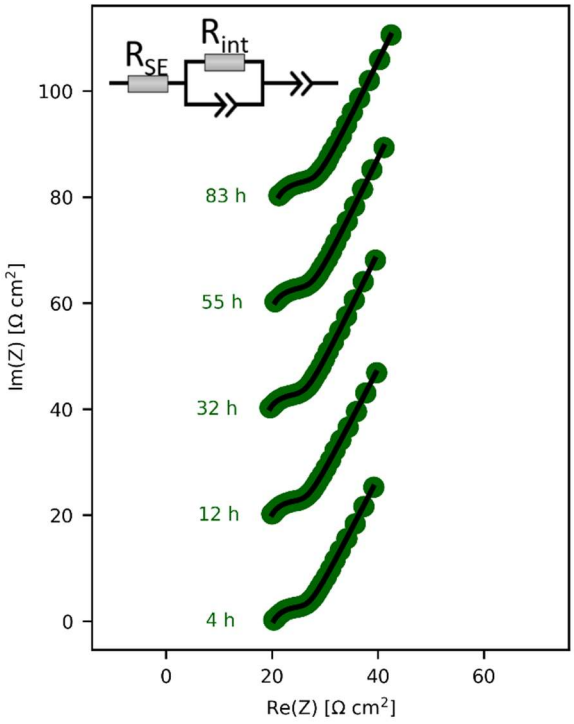

Figure S2. Exemplary impedance spectra of the 2D silicon electrode after lithiation to -0.6 V vs In/InLi, i.e. 22 mV vs Li^+/Li, and their fit with the equivalent circuit shown on the top left. Each spectrum is offset on the vertical axis for better readability. The equivalent circuit used for fitting is shown as an insert. The data points used for fitting are shown (from 200 Hz to 5 mHz).

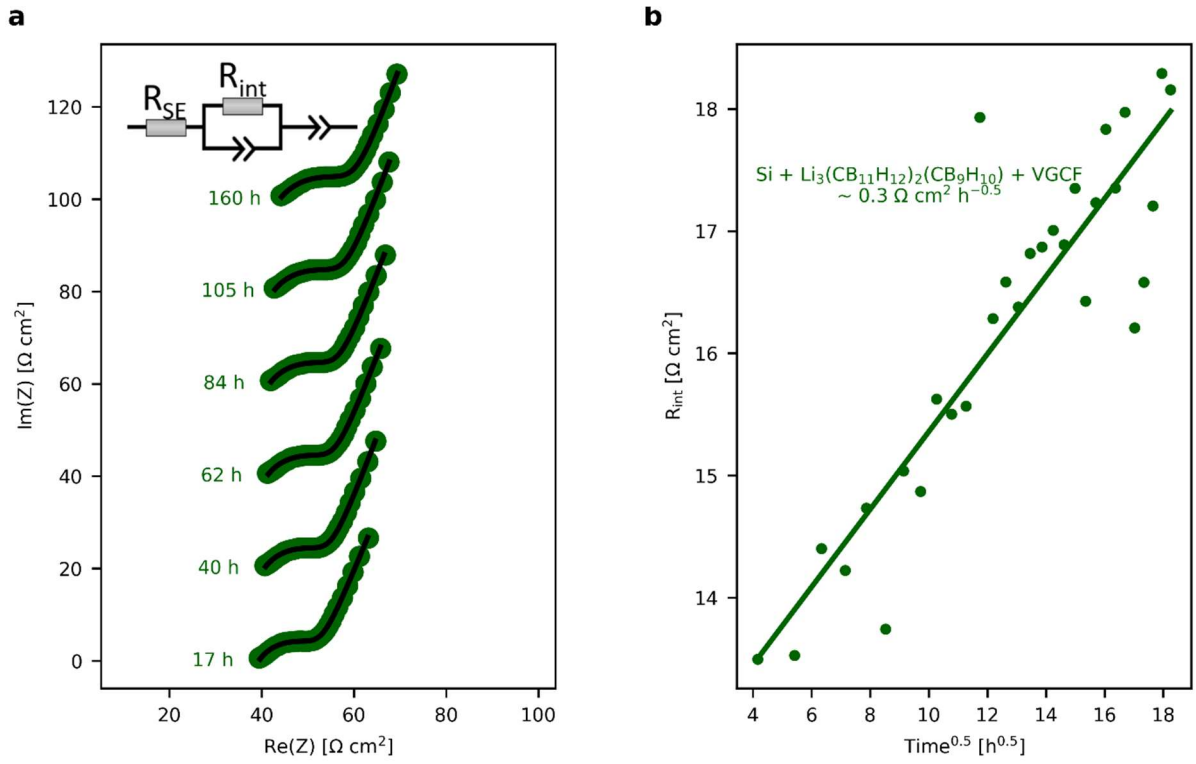

Figure S3. a) Exemplary impedance spectra and their fit of the 3D silicon composite electrode with vapor-grown carbon fibers (VGCF) after lithiation to -0.6 V vs In/InLi, i.e. 22 mV vs Li^+/Li. Each spectrum is offset on the vertical axis for better readability. The equivalent circuit used for fitting is shown as an insert. The data points used for fitting are shown (from 200 Hz to 5 mHz). **b)** Fitted interface resistance R_{int} as a function of the square-root of time, as well as linear fit with corresponding interface resistance growth rate.

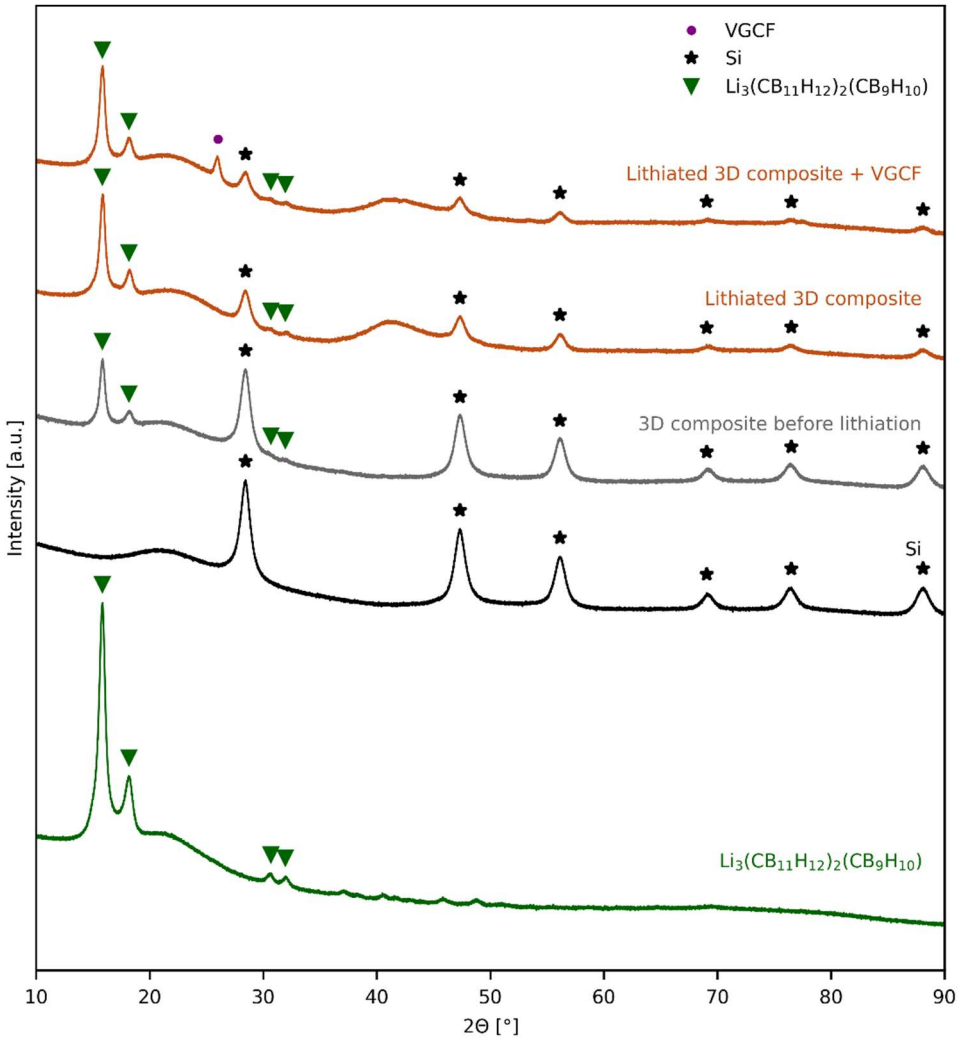

Figure S4. X-ray diffraction patterns for 3D silicon composite electrodes before lithiation (gray) and after lithiation (orange), and corresponding patterns for pristine silicon nanoparticles (black) and $Li_3(CB_{11}H_{12})_2CB_9H_{10}$ solid electrolyte (green). The peak marked with a purple circle can be attributed to the vapor-grown carbon fibers (VGCF), which were measured separately. A square-root scaling was applied to the intensity values to enhance readability. The patterns are vertically offset for better readability.

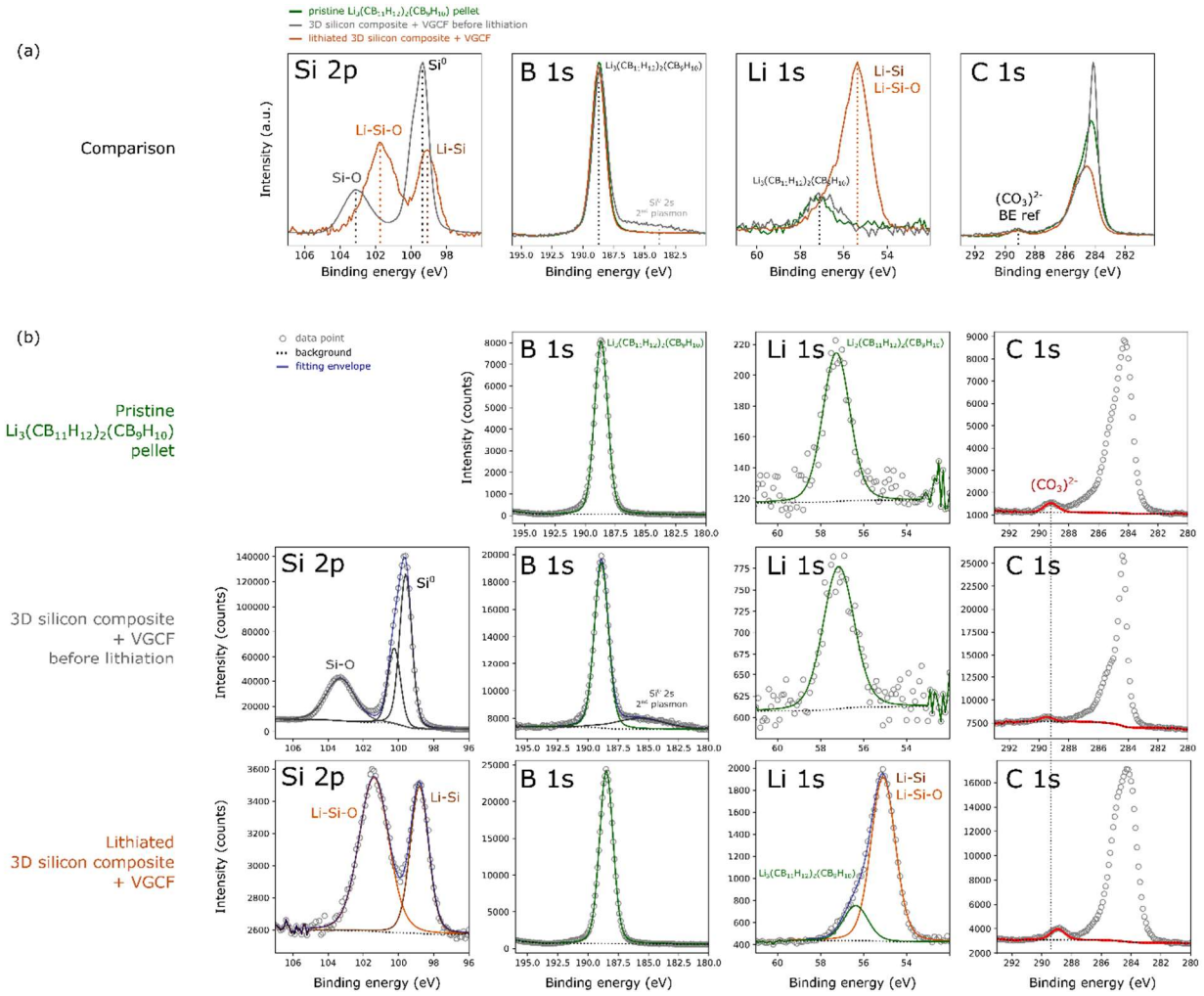

Figure S5. a) XPS spectra comparing the Si 2p, B 1s, Li 1s, and C 1s core-levels for pristine $Li_3(CB_{11}H_{12})_2CB_9H_{10}$ solid electrolyte (green), for the 3D silicon composite electrode with carbon fibers before lithiation (gray) and for the 3D silicon composite electrode with carbon fibers after lithiation (orange). For charge compensation, binding energies were corrected to align the $(CO_3)^{2-}$ peak position. To enable comparison across samples, intensities are normalized to the solid electrolyte B 1s peak area, except for the Si 2p region, for which spectra were instead normalized by setting the integrated total signal intensity to unity (for better visualization of the Si 2p signal of the 3D silicon composite electrode with carbon fibers after lithiation). Native silicon oxides are present on the silicon particles. **b)** Corresponding measured data points and fits before any binding energy correction or intensity normalization. The C 1s spectra are only partially fitted because the constituent chemical environments in the 282-288 eV region could not be unambiguously attributed.

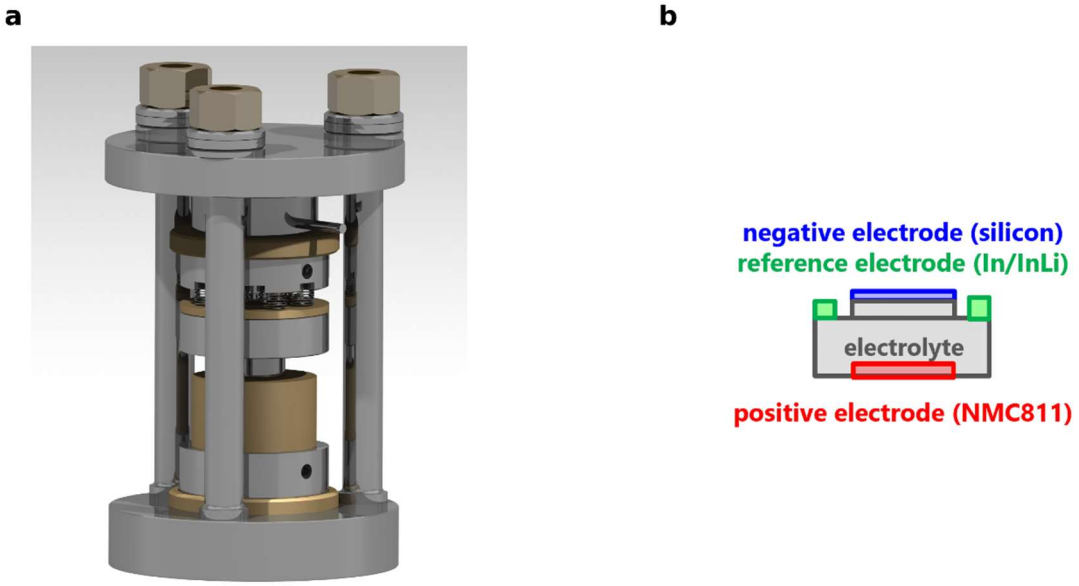

Figure S6. a) Rendering of the three-electrode pressure cell in its frame. **b)** Corresponding schematic of the cell cross-section with silicon negative electrode, NMC888 positive electrode and ring-shaped In/InLi reference electrode.

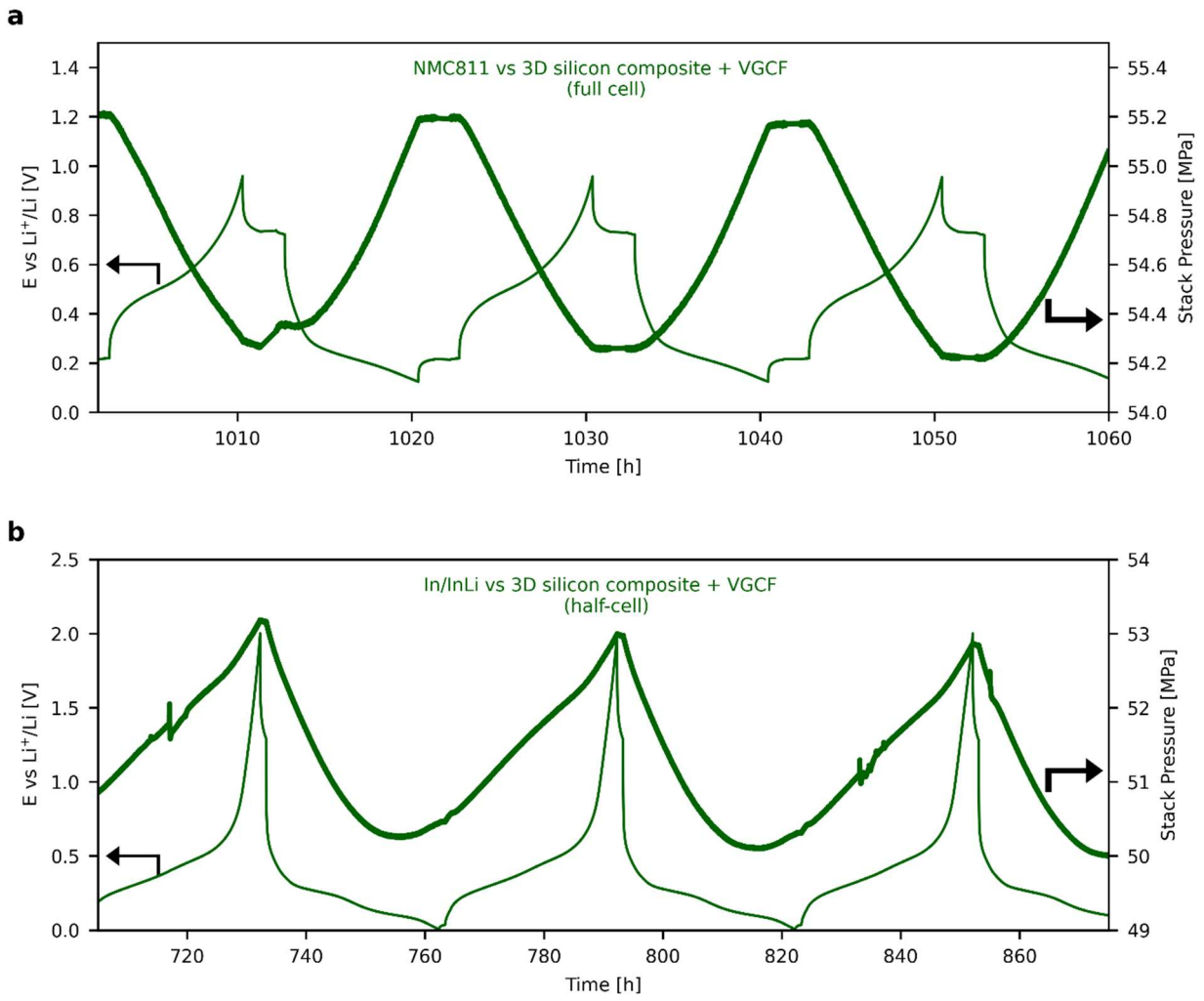

Figure S7. Time evolution of stack pressure during cycling (thick lines, right vertical axis), as well as time evolution of the silicon electrode potential (thin lines, left vertical axis), for **a)** NMC811 vs 3D silicon composite full cells as presented in Figure 3 and **b)** In/InLi vs 3D silicon composite half-cells as presented in Figure 2.

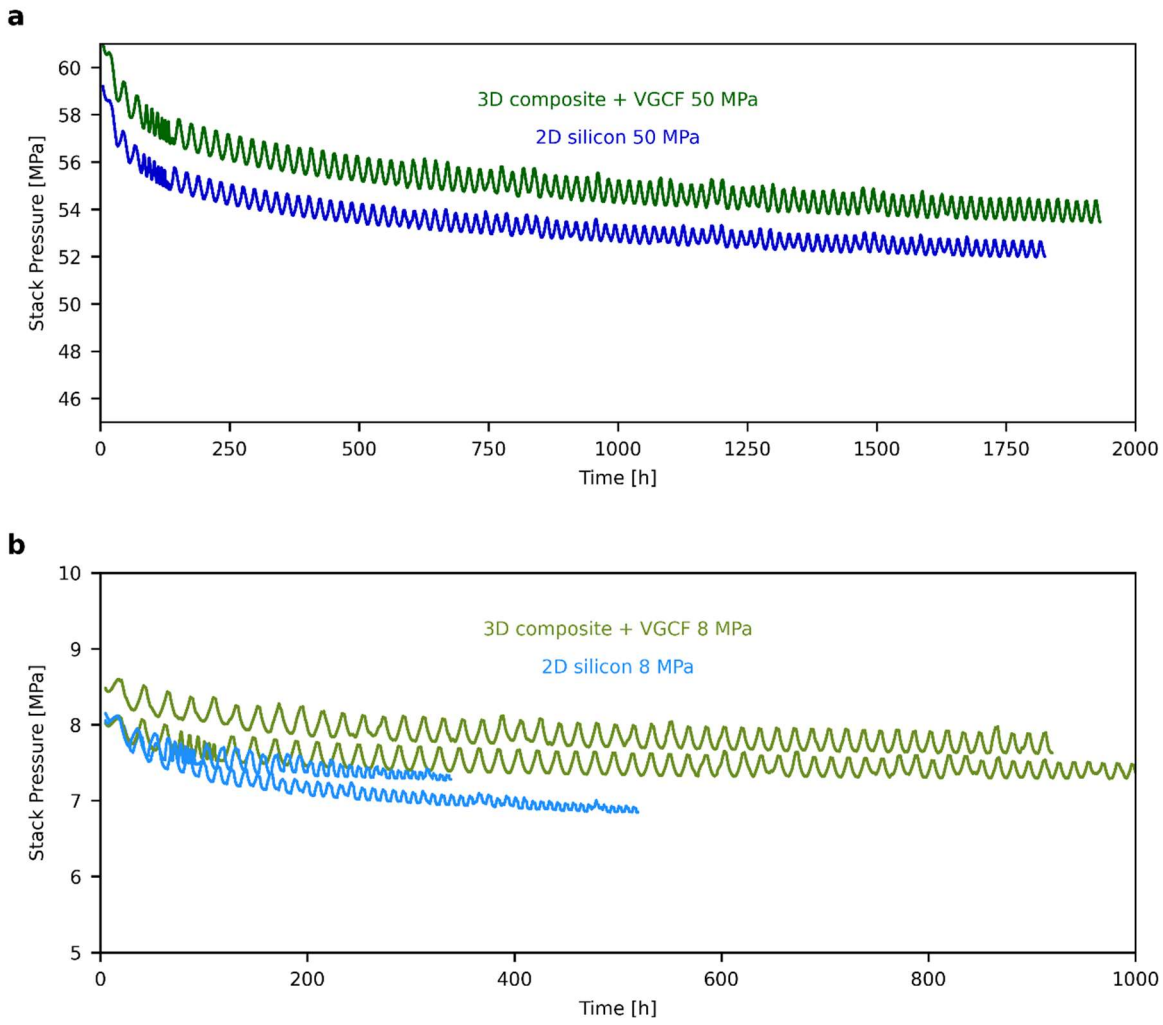

Figure S8. Evolution of stack pressure during cycling of NMC811 vs silicon full cells under a nominal pressure of **a)** 50 MPa as presented in Figure 3 and **b)** 8 MPa as presented in Figure 4.

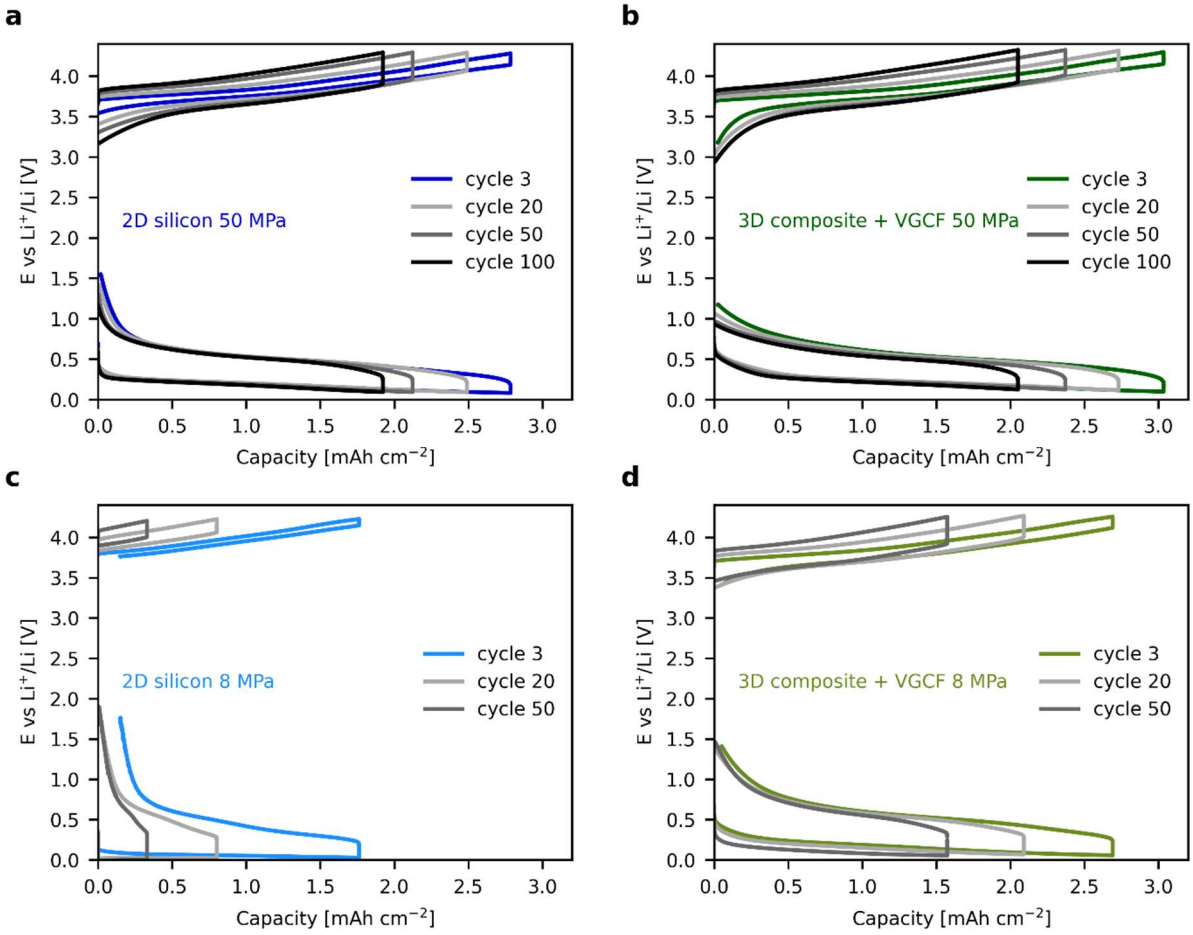

Figure S9. Electrode potential profiles at 0.3 mA cm^{-2} for selected cycles under **a), b)** 50 MPa and **c), d)** 8 MPa.

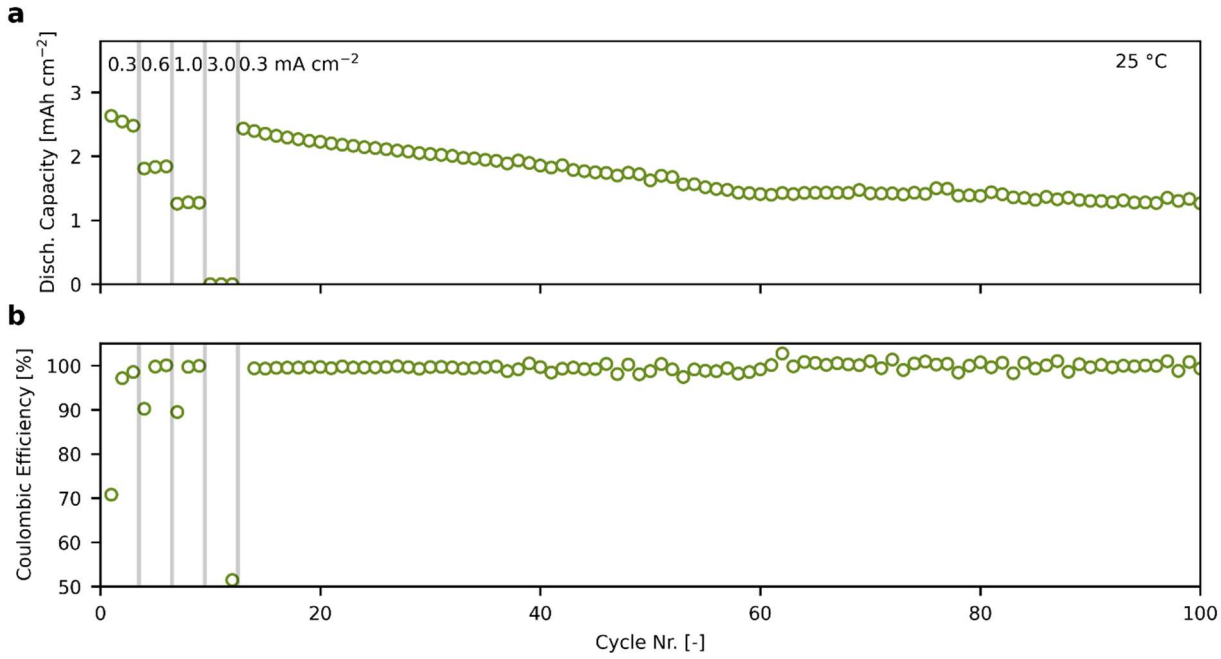

Figure S10. a) Discharge capacity and **b)** coulombic efficiency of solid-state cells with NMC811 positive electrode and 3D silicon composite negative electrode, cycled under 8 MPa stack pressure for 100 cycles.

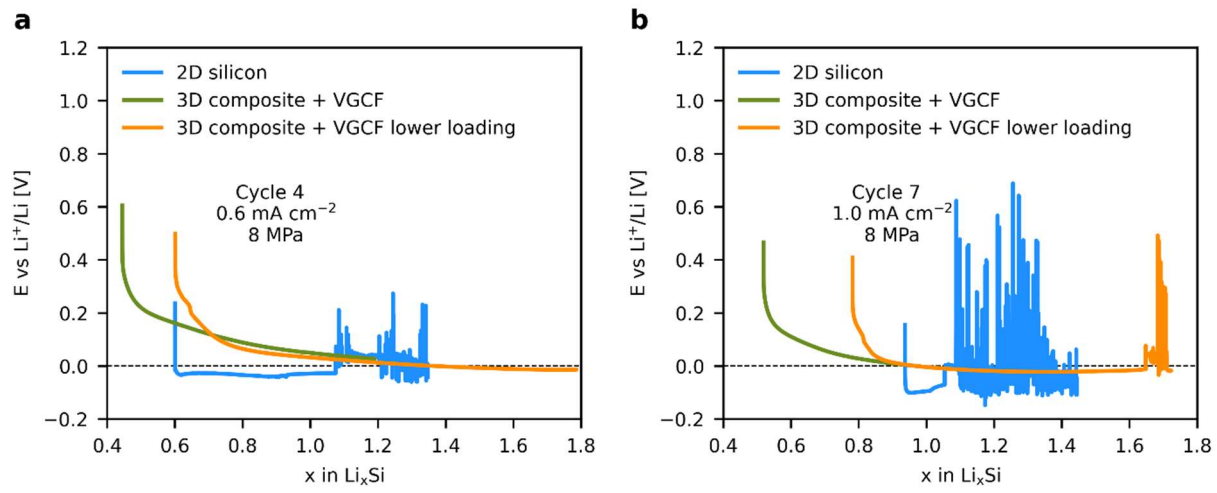

Figure S11. Potential profiles during lithiation under 8 MPa stack pressure at a current density of **a)** 0.6 mA cm^{-2} and **b)** 1.0 mA cm^{-2}. The silicon composite (light green) and solid-electrolyte-free silicon electrodes (light blue) feature the standard active material loading of 2.8 mg_{Si} cm^{-2}, and the silicon composite electrode with lower active material loading of 2.0 mg_{Si} cm^{-2} is marked in orange.

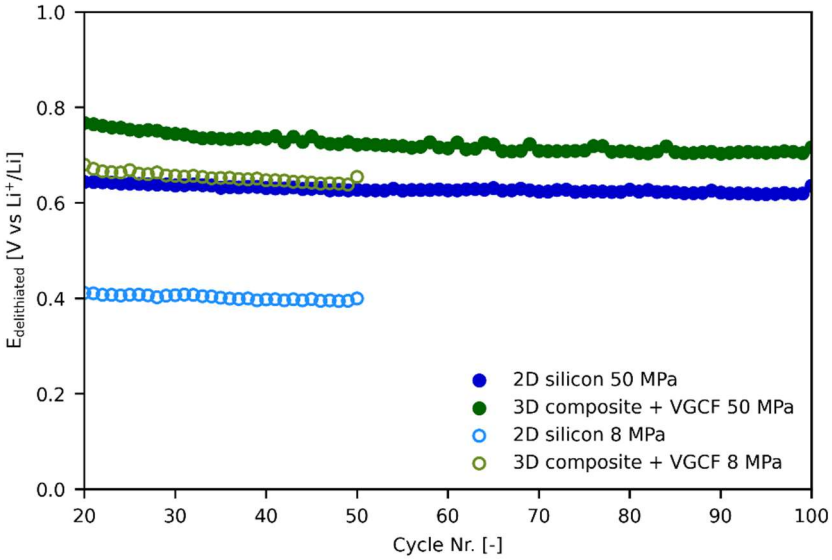

Figure S12. Open-circuit potentials of silicon electrodes, 90 min after end of delithiation (discharge).

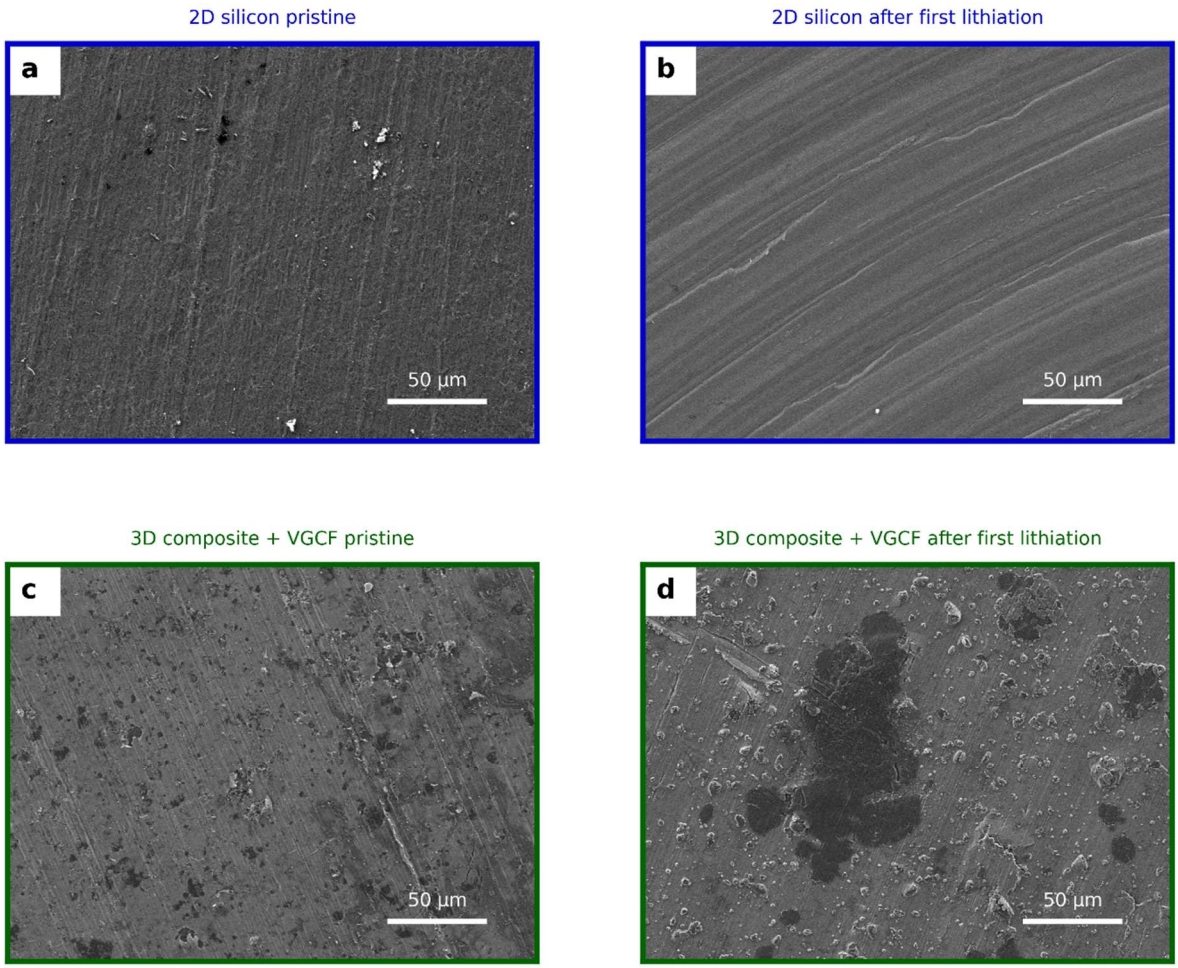

Figure S13. Scanning electron microscopy images in top view for representative **a)** 2D silicon electrodes before cell cycling, **b)** 2D silicon electrodes after the first lithation at 50 MPa, **c)** 3D silicon composite electrodes before cell cycling, **d)** 3D silicon composite electrodes after the first lithation at 50 MPa. The electrodes in a) and c) are representative for the cells cycled at 50 MPa and also for the cells cycled at 8 MPa, because the cell assembly procedure is independent of the cycling stack pressure. The concentric marks on the surface are attributed to the surface roughness of the stainless steel pressure cell, which was machined with a turning process.

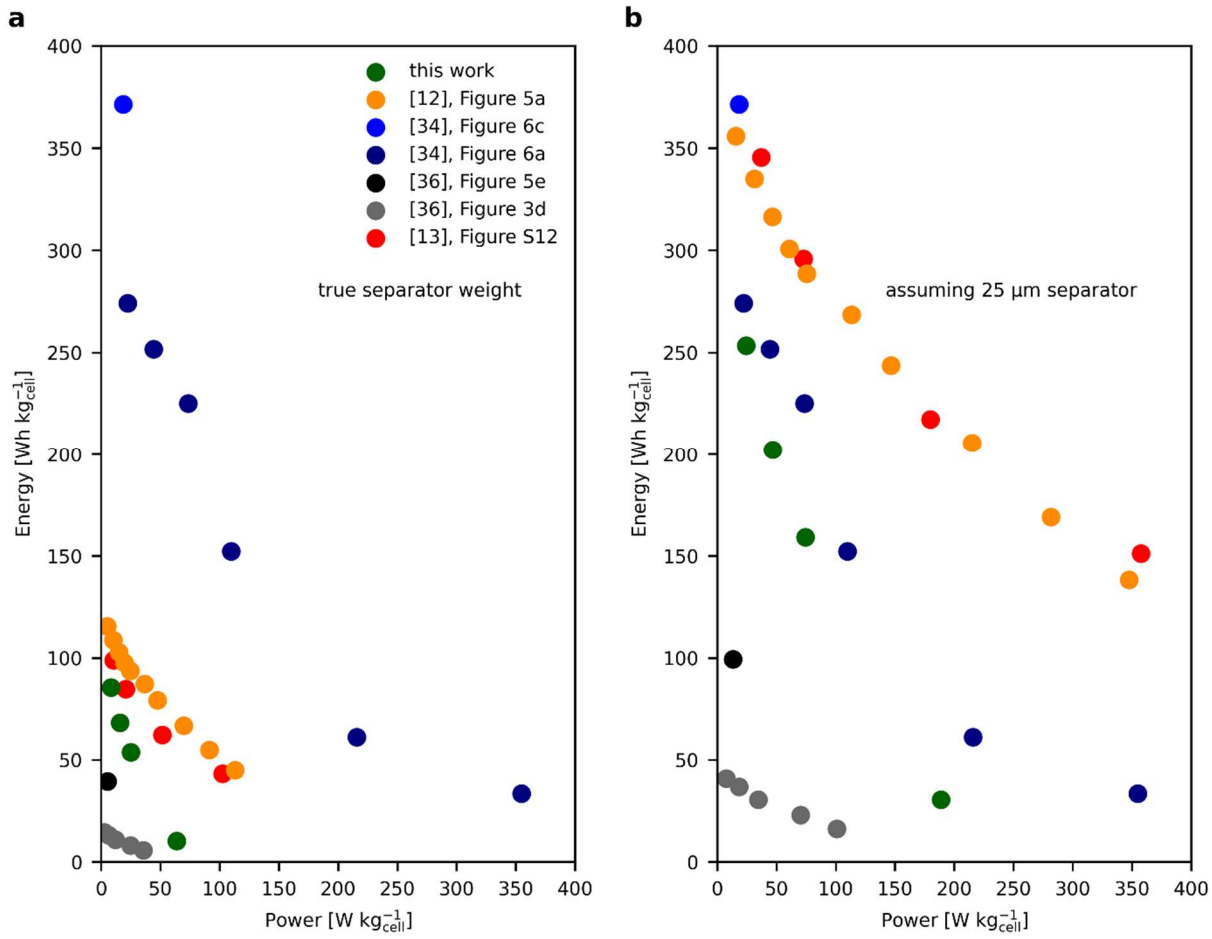

Figure S14. Comparison of the hydroborate full cell with 3D silicon composite electrode under 50 MPa stack pressure presented in this work to some recently published solid-state batteries with Li_6PS_5Cl, polymer, and halide electrolytes, in terms of specific energy and specific power, calculated with **a)** the true separator weight and **b)** the separator weight assuming a separator thickness of 25 µm. The values used for calculation are presented in Table S1.

Table S1. Values used for the calculation of specific energy and power

		Unit	This work	[12]	[13]	[34]	[36]
electrolyte		-	$Li_3(CB_{11}H_{12})_2(CB_9H_{10})$	Li_6PS_5Cl	Li_6PS_5Cl	polymerized ionic liquid	$Li_2In_{1/3}Sc_{1/3}Cl_4$ bilayer with $Li_{6.7}Si_{0.7}Sb_{0.3}I$
electrolyte density	ρ	g cm^{-3}	1.1	1.64	1.64	1.6	2.49
cell diameter		mm	12.5 (two-electrode cells)	10	10	12	10
True separator weight	w_{sep}	mg cm^{-2}	81.5	95.5	101.9	3.2	178.3
Separator weight assuming 25 µm $w_{sep,25µm} = ρ*25$ µm	$w_{sep,25µm}$	mg cm^{-2}	2.75	4.1	4.1	3.2	6.2
negative electrode			nanosilicon composite	micro-silicon	micro-silicon	20 µm lithium metal	In/InLi
neg. electrode active material loading		mg cm^{-2}	2.83	1.67	1.6	1.1	74.1
wt% active material in neg. electrode		%	54.5	99.9	99.5	100	100
weight neg. electrode	w_{neg}	mg cm^{-2}	5.2	1.67	1.6	1.1	74.1
weight Cu current collector 10 µm	w_{Cu}	mg cm^{-2}	8.96	8.96	8.96	8.96	8.96
positive electrode			$LiNi_{0.8}Co_{0.1}Mn_{0.1}O_2$	$LiNi_{0.8}Co_{0.1}Mn_{0.1}O_2$	$LiNi_{0.83}Co_{0.11}Mn_{0.06}O_2$	$LiNi_{0.8}Co_{0.1}Mn_{0.1}O_2$	$LiNi_{0.85}Co_{0.1}Mn_{0.05}O_2$
pos. electrode active material loading		mg cm^{-2}	18.4	25	21.5	Fig. 6a: 6.3 Fig. 6c: 16.1	Fig. 3d: 6.2 Fig. 5e: 21.6
wt% active material in pos. electrode		%	70	77.3	77.7	86	80
weight pos. electrode	w_{pos}	mg cm^{-2}	26.3	32.3	27.7	Fig. 6a: 6.7 Fig. 6c: 18.9	Fig. 3d: 7.8 Fig. 5e: 27
weight Al current collector 10 µm	w_{Al}	mg cm^{-2}	2.7	2.7	2.7	2.7	2.7
total weight $w_{tot} = 0.5*w_{Cu} + w_{neg} + w_{sep} + w_{pos} + 0.5*w_{Al}$	w_{tot}	**mg cm^{-2}**	**119**	**135**	**137**	**Fig. 6a: 17 Fig. 6c: 29.6**	**Fig. 3d: 266 Fig. 5e: 285**
total weight with 25 µm separator $w_{tot,25µm} = 0.5*w_{Cu} + w_{neg} + w_{sep,25µm} + w_{pos} + 0.5*w_{Al}$	$w_{tot,25µm}$	**mg cm^{-2}**	**40**	**44**	**39**	**Fig. 6a: 17 Fig. 6c: 29.6**	**Fig. 3d: 94 Fig. 5e: 113**

		Unit	This work	[12]	[13]	[34]	[36]
current densities	j	mA cm^{-2}	[0.3, 0.6, 1.0, 3.0]	[0.2, 0.4, 0.6, 0.8, 1.0, 1.5, 2.0, 3.0, 4.0, 5.0]	[0.43, 0.86, 2.15, 4.3]	Fig. 6a: [0.1, 0.2, 0.33334, 0.5, 1.0, 2.0, 5.0] Fig. 6c: [0.14]	Fig. 3d: [0.224, 0.56, 1.12, 2.24, 3.36] Fig. 5e: [0.49]
capacity	q	mAh cm^{-2}	[3.11, 2.59, 2.14, 0.49]	[4.51, 4.26, 4.09, 3.95, 3.82, 3.55, 3.32, 2.87, 2.4, 1.99]	[4.01, 3.49, 2.6, 1.82]	Fig. 6a: [1.23, 1.13, 1.02, 0.69, 0.28, 0.19, 0.13] Fig. 6c: [2.8]	Fig. 3d: [1.21, 1.12, 0.99, 0.73, 0.54] Fig. 5e: [3.68]
average cell potential	U_{avg}	V	[3.27, 3.13, 2.99, 2.52]	[3.47, 3.45, 3.4, 3.35, 3.32, 3.32, 3.22, 3.15, 3.09, 3.06]	[3.38, 3.32, 3.28, 3.26]	Fig. 6a: [3.77, 3.75, 3.72, 3.71, 3.64, 2.99, 2.99] Fig. 6c: [3.85]	Fig. 3d: [3.17, 3.08, 2.9, 2.95, 2.82] Fig. 5e: [3.05]
Energy $E = q * U_{avg}$	**E**	**mWh cm^{-2}**	**[10.2, 8.1, 6.4, 1.2]**	**[15.6, 14.7, 13.9, 13.2, 12.7, 11.8, 10.7, 9.0, 7.4, 6.1]**	**[13.6, 11.6, 8.5, 5.9]**	**Fig. 6a: [4.6, 4.2, 3.8, 2.6, 1.0, 0.6, 0.4] Fig. 6c: [10.78]**	**Fig. 3d: [3.8, 3.4, 2.9, 2.2, 1.5] Fig. 5e: [11.2]**
Average Power $P_{avg} = U_{avg} * j$	**P_{avg}**	**mW cm^{-2}**	**[1.0, 1.9, 3.0, 7.6]**	**[0.7, 1.4, 2.0, 2.7, 3.3, 5.0, 6.4, 9.4, 12.4, 15.3]**	**[1.5, 2.9, 7.1, 14.0]**	**Fig. 6a: [0.4, 0.7, 1.2, 1.9, 3.6, 6.0, 15.0] Fig. 6c: [0.5]**	**Fig. 3d: [0.7, 1.7, 3.2, 6.6, 9.5] Fig. 5e: [1.5]**